Deep-Sea Research II 117 (2015) 41–52

Contents lists available at ScienceDirect

Deep-Sea Research II

journal homepage: www.elsevier.com/locate/dsr2

A modeling study of the formation, maintenance, and relaxation of upwelling circulation on the Northeastern South China Sea shelf

Jianping Gan [a,*], Jingjing Wang [a], Linlin Liang [a], Li Li [b], Xiaogang Guo [b]

[a] Department of Mathematics & Division of Environment, Hong Kong University of Science and Technology, Hong Kong, China
[b] The Third Institute of Oceanography, State Oceanic Administration, China

ARTICLE INFO

Available online 15 January 2014

Keywords:
Wind-driven upwelling dynamics
Geostrophic cross-isobath transport
Circulation over variable shelf

ABSTRACT

We investigated persistent summer upwelling circulation, in response to upwelling and downwelling favorable winds, in the Northeastern South China Sea (NSCS). We used a validated three-dimensional ocean circulation model that was forced by realistic atmospheric fluxes and downscaled coupling of real-time lateral fluxes. We found that upwelling in the NSCS was formed and maintained by the presence of an intensified westward along-isobath pressure gradient force (PGF_m) and bottom frictional effect that led to cross-isobath currents over the unique NSCS widened shelf. The upwelling favorable PGF_m and the frictional effect arose from the interaction between the eastward shelf current and the shelf topography. These intrinsic upwelling dynamics in the NSCS were largely sustained during episodic downwelling winds in the upwelling season because the retreat of the eastward shelf current from pre-existing upwelling was significantly slowed by the unique widened shelf topography. Furthermore, the upwelling dynamics could also be maintained and, even developed, during downwelling favorable winds, when the eastward shelf current was sustained by the pumping of downstream outflow.

1. Introduction

Spatiotemporal variation of upwelling circulation over a continental shelf can be induced by various forcing mechanisms. It is well known that the presence of alongshore topographic variations on an otherwise relatively straight continental shelf has a profound influence on coastal upwelling circulation (Lentz et al., 1999; Gan and Allen, 2005a; Barth et al., 2005; Weisberg et al., 2005; Gan et al., 2009a, 2010). These studies showed that interaction between the upwelling flow and variable shelf topography alters both alongshore and cross-shore momentum balances and leads to strong variability in upwelling circulation. A variable wind field can also form highly variable coastal upwelling circulation. For example, it occurs when an upwind current is formed by the relaxation of upwelling winds (Send et al., 1987; Gan and Allen, 2002) or when enhanced spatial variability of the upwelling intensity is caused by a spatially variable wind stress field (Gan et al., 2005; Castelao and Barth, 2007). Meanwhile, remote currents and wave intrusion from the region beyond the shelf also exert additional variance and forcing on the upwelling circulation over the shelf (e.g. Chapman, 1987; Denbo and Allen, 1987; Pringle and Dever, 2009).

The topography of the Northeastern South China Sea (NSCS) is characterized by a complex variable coastline in the nearshore region and by a prominent eastward widened shelf. The widened shelf is formed by an abrupt offshore extension of isobaths east of the Pearl River Estuary and is bounded by the 50 m isobath at its southern edge (Fig. 1). Gan et al. (2009a) examined the response of the monsoon-driven coastal upwelling circulation effected by this unique topography and found that the upwelling intensified over the widened shelf because of a strengthened bottom Ekman transport and shoreward cross-isobath geostrophic transport. This kind of topographic control of shelf upwelling was also reported in many other studies (e.g. Lentz et al., 1999; Janowitz and Pietrafesa, 1982; Oke and Middleton, 2000; Weisberg et al., 2000; Gan and Allen, 2002, 2005a; Pringle, 2002). While the apparent source for the intensified bottom frictional transport was the strengthened shelf current over the converging isobaths at the head of the widened shelf, the source for intensified geostrophic transport was provided by the along-isobath pressure gradient due to net stress curl in the water column (Gan et al., 2013.)

In general, under the influence of the East Asian monsoon, southwesterly upwelling favorable winds prevail over the NSCS during the summer in June, July, and August (Li, 1993). However, in the summer of 2000, this upwelling favorable wind was not remarkable over the NSCS (Fig. 2). The average magnitude of the upwelling favorable wind stress was weakened by episodic downwelling favorable winds (Fig. 3). The time series of alongshore

* Corresponding author.
E-mail address: magan@ust.hk (J. Gan).

0967-0645/$ - see front matter © 2014 Elsevier Ltd. All rights reserved.
http://dx.doi.org/10.1016/j.dsr2.2013.12.009

wind stress at locations P1–P6 (Fig. 1) from June 5 to August 24, 2000 (Fig. 3) demonstrate the spatial differences of wind stress and show that all series correlate well. The figure also reveals that the upwelling favorable wind seldom occurred from June 20 to July 22, 2000. From June 5 to August 24, the total number of days with upwelling favorable and downwelling favorable winds was roughly the same, yet the coastal upwelling phenomenon dominated over the shelf in the NSCS for the entire period. The average upwelling feature over this period is demonstrated by the existence of cold sea surface temperature (SST) as seen from the remotely sensed data (Fig. 2), similar to the upwelling feature when winds were persistently upwelling favorable shown in Gan et al. (2009a). In spite of the stronger southwesterly winds existed over the western part of the shelf, the colder upwelled water occurred over the eastern part. Similarly, the standard deviation of wind stress in Fig. 2 shows the existence of highly variable wind stress near the head of the widened shelf, while the higher variance of SST appeared near the coastal promontory off Shantou. These statistics suggest that the upwelling occurred persistently in the NSCS during summer; and that the upwelling circulation in the NSCS was not formed and sustained by upwelling-favorable wind forcing alone. Other unknown forcing mechanisms, such as the flow-topography dynamics of the widened shelf and remote inflow/outflow, may also play important controlling roles, as was pointed out by Gan et al. (2009a,b).

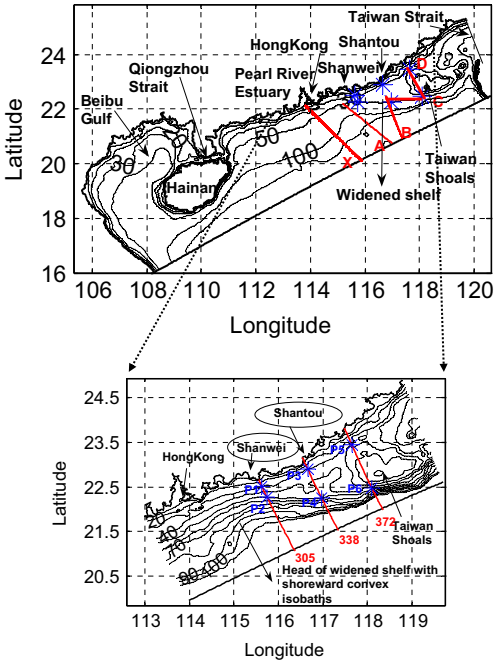

Fig. 1. The topography (m) in the NSCS with the zoomed area at the widened shelf. The five transects marked with X, A, B, C, and D represent the locations of observed data transects during summer cruises in 2000. The selected cross-shelf sections (dashed lines) are marked by their grid numbers 305, 338, and 372. The shoreward convex isobaths are at the head of the widened shelf about one half degree southwest of Shanwei. Six locations selected for this study are P1, P3, and P5 along the 30 m isobath with the corresponding grid numbers 305, 338, and 372 as well as P2, P4, and P6 along the 50 m isobath with the same grid numbers.

In this study, we used a three-dimensional numerical ocean model, with realistic atmospheric fluxes and real-time lateral fluxes produced by downscaled coupling, to investigate the unknown forcing processes that sustained the persistent summer upwelling circulation in the NSCS during both upwelling and downwelling favorable winds.

2. Ocean model

The NSCS ocean model (Gan et al., 2009a,b, 2010) is based on the Regional Ocean Model System (ROMS) (Shchepetkin and McWilliams, 2005) for three-dimensional, time-dependent oceanographic flows that are governed by hydrostatic primitive equations. A local closure scheme based on the level-2.5 turbulent kinetic energy equations by Mellor and Yamada (1982) was adopted in the vertical mixing parameterization. The model domain extends from 15.99°N, 108.17°E in the southwest corner to about 25.81°N, 119.54°E in the northeast corner with its central axis directed 23° anticlockwise from true east (Fig. 1). We used a curvilinear grid (x,y) with an average 3 km horizontal grid size. Thirty levels of stretched, generalized, terrain-following coordinates (s) form minimum and maximum grid spacing in the water column with less than 1 m over the inner shelf and

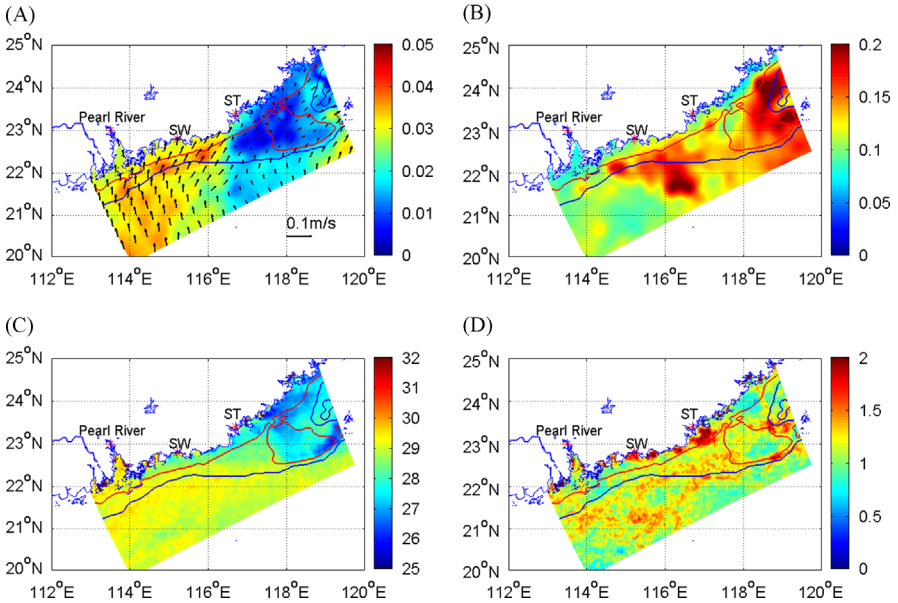

Fig. 2. (a) Averaged QuikScat wind stress vectors (Pa) and magnitude (color contours); (b) standard deviation of wind stress vector magnitude, (c) averaged MODIS SST (°C) and (d) its standard deviation of SST for days 20–100 (June 5–August 24) in the NSCS. The 30 m and 50 m isobaths are shown as red and blue contour lines, respectively. (For interpretation of the references to color in this figure legend, the reader is referred to the web version of this article.)

~10 m over the outer slope, respectively. Water depths, $H(x,y)$, were obtained by merging ETOPO2 (1/30°) from the National Geophysical Data Center (USA) with depths that were digitized from navigation maps published by the Maritime Safety Administration (China).

The NSCS model was initialized with zero velocities and average three-dimensional temperature and salinity fields, from April 16 to May 16, 2000, obtained from the South China Sea (SCS) circulation model (Gan et al., 2006). The SCS model is a three-dimensional circulation model based on the Princeton Ocean Model and has an average 10 km horizontal grid size and 30 levels of terrain-following coordinates. Both the SCS and NSCS models were forced with daily QuikScat wind stress that had $\frac{1}{4}^\circ$ resolution and heat flux that was calculated by a bulk atmospheric formula based on 6-hourly $1\times1^\circ$ NCEP reanalysis atmospheric variables. Daily observed discharge in the Pearl River was applied at the upper Pearl River Estuary. The NSCS model was nested with the real time variables of daily averaged depth-integrated velocity (U,V), depth-dependent velocities (u,v), temperature (T), and salinity (S) taken from the SCS circulation model at the eastern and southern boundaries. We used active open boundary conditions (OBCs) for the model variables U, V, u, v, T, and S along the open boundaries (Gan and Allen, 2005b). The OBCs integrate the outer forcing information into the limited-area domain while allowing the disturbances generated inside the domain to travel outward across the open boundaries without spurious reflection. The NSCS simulation started on May 16 and the model output used for this analysis was from June 5 to August 24, 2000.

3. Model results

3.1. Observation-model comparison

Five conductivity–temperature–depth (CTD) transects were sampled over the eastern part of the widened shelf (Fig. 1) during cruises on July 19–21 and July 30–31, 2000. Real-time comparisons of the simulated horizontal temperature fields with observations during the cruise periods are shown in Figs. 4 and 5 and the corresponding comparisons along three cross-shelf sections X, A, and B are shown in Fig. 6.

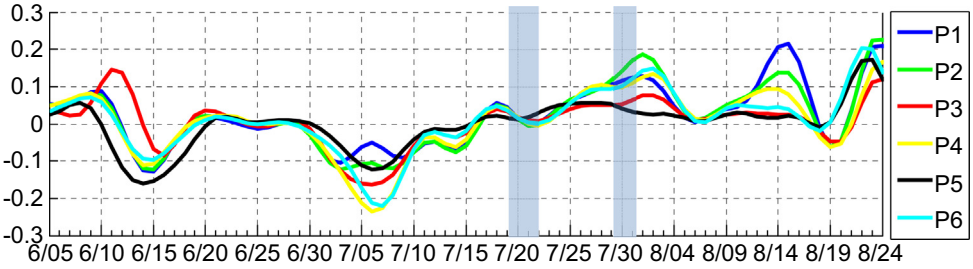

Fig. 3. The time series of alongshore wind stress (Pa) at six locations P1–P6 (refer to Fig. 1) for days 20–100 (June 5–August 24). Sampling periods of field measurements from July 19–21 and July 30–31 are shaded. The positive and negative values are for the northeastward upwelling-favorable and southwestward downwelling-favorable wind stress, respectively.

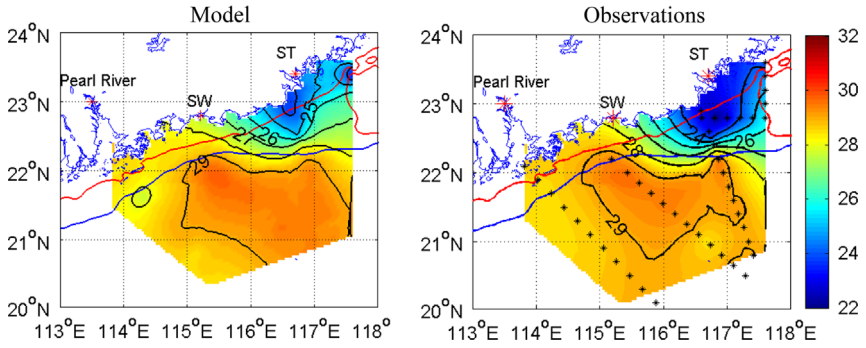

Fig. 4. Temperature (°C) at 5 m from the ensemble results of CTD transects (right) and from the model (left).

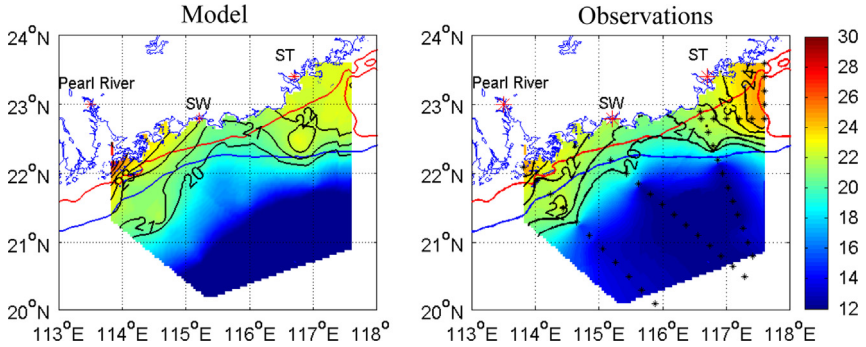

Fig. 5. Same as Fig. 4, but for the bottom temperature (°C).

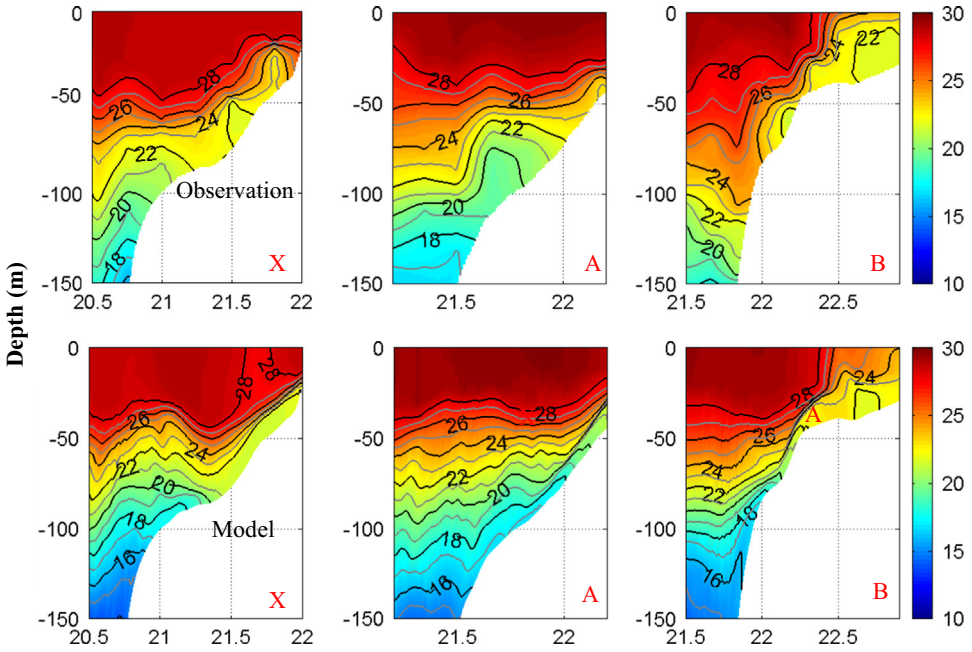

Fig. 6. Cross-shore sections of temperature (°C) along the transects from the observations (top) and from the model (bottom).

The average observed temperature field at 5 m matches the corresponding simulated one very well (Fig. 4). The upwelled cold water was found over the widened shelf with relatively cold water around Shantou. Although the model's temperatures were slightly warmer, the spatial distribution was highly consistent with the observations. Tides, which were not included in the model, would have further cooled the surface water, in particular, near Taiwan Strait where the magnitude of the M_2 tide is strong. At the sea bottom, both model output and observations showed that the temperature was generally distributed along the isobaths: higher over the shelf while lower in the deep ocean (Fig. 5). Both exhibited a distinct cold bottom water intrusion near the head of the widened shelf.

In the cross-shelf sections, along transects X, A, and B (Fig. 6), both the simulated results and observations reveal that cold water from depths down to 100 m advected upward and shoreward over the slope of the shelf. The sampling along section X was conducted during weak upwelling favorable winds from July 19 to 21, after a long duration of downwelling favorable winds (Fig. 3). The isotherms advanced shoreward in the bottom layer over the slope and the feature was captured in the model simulation. Relatively strong upslope cold water advection along section A represented a strong shoreward invasion of deep water, not only because of the strong upwelling winds during the sampling period of July 30, but also because of the shoreward convex isobaths at the head of the widened shelf (Fig. 1; Gan et al., 2009a). This shoreward intrusion was also observed in our model results but with a slightly thinner bottom boundary layer. Both results showed that no upwelled cold water outcropped in the nearshore along section A. For section B, the cold water that outcropped near the shore was not connected with the water mass in the deeper water offshore in the section, implying the downstream advection of cold water from the head of the widened shelf. This feature was also seen in the model results and confirmed what was found by Gan et al. (2009a). Those authors indicated that the relatively cold (22°C) coastal water off Shantou near section B was originated upstream near the convex isobaths, and subsequently advected eastward and shoreward downstream by the alongshore upwelling current.

By careful examination of the response at section X, we see the prominent upslope advection over the mid-shelf region in both

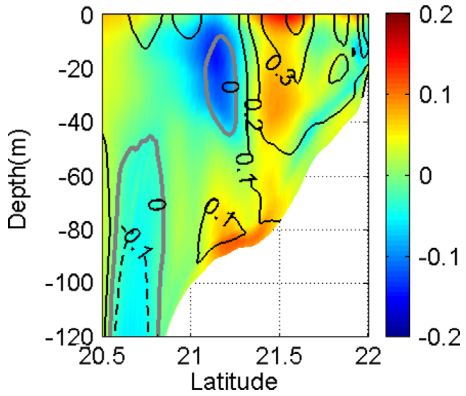

Fig. 7. Model results of the alongshore velocity, u (m s^{-1}, black contour line with positive value referring to the eastward current.), and cross-shore velocity, v (m s^{-1}, color contours with positive value referring to the shoreward current), at across-shore transect X from July 19–21. The thick gray contours refer to zero alongshore velocity. (For interpretation of the references to color in this figure legend, the reader is referred to the web version of this article.)

temperature (Fig. 6) and velocity transects (Fig. 7), in spite of a long period of downwelling favorable wind forcing immediately before the sampling on July 19 (Fig. 3). The upwelling evident in the cold SST field (Fig. 2), the shoreward cross-shore bottom velocity and the positive (eastward) alongshore current during the relaxation of the downwelling wind (Fig. 7) suggest that wind forcing alone cannot account for the upwelling on the shelf. A similar occurrence of upwelling circulation during downwelling favorable winds was also observed in the field measurements in the region during a 2008 cruise (not shown). Dynamic processes, such as the dissipation/maintenance of a pre-existing upwelling dynamics and the forcing of remote inflow/outflow, play an important role in the maintenance and formation of the upwelling circulation in the NSCS, as to be shown below.

3.2. Mean flow

The general characteristics of the flow response to the wind-driven shelf circulation are shown by horizontal fields of (u,v)

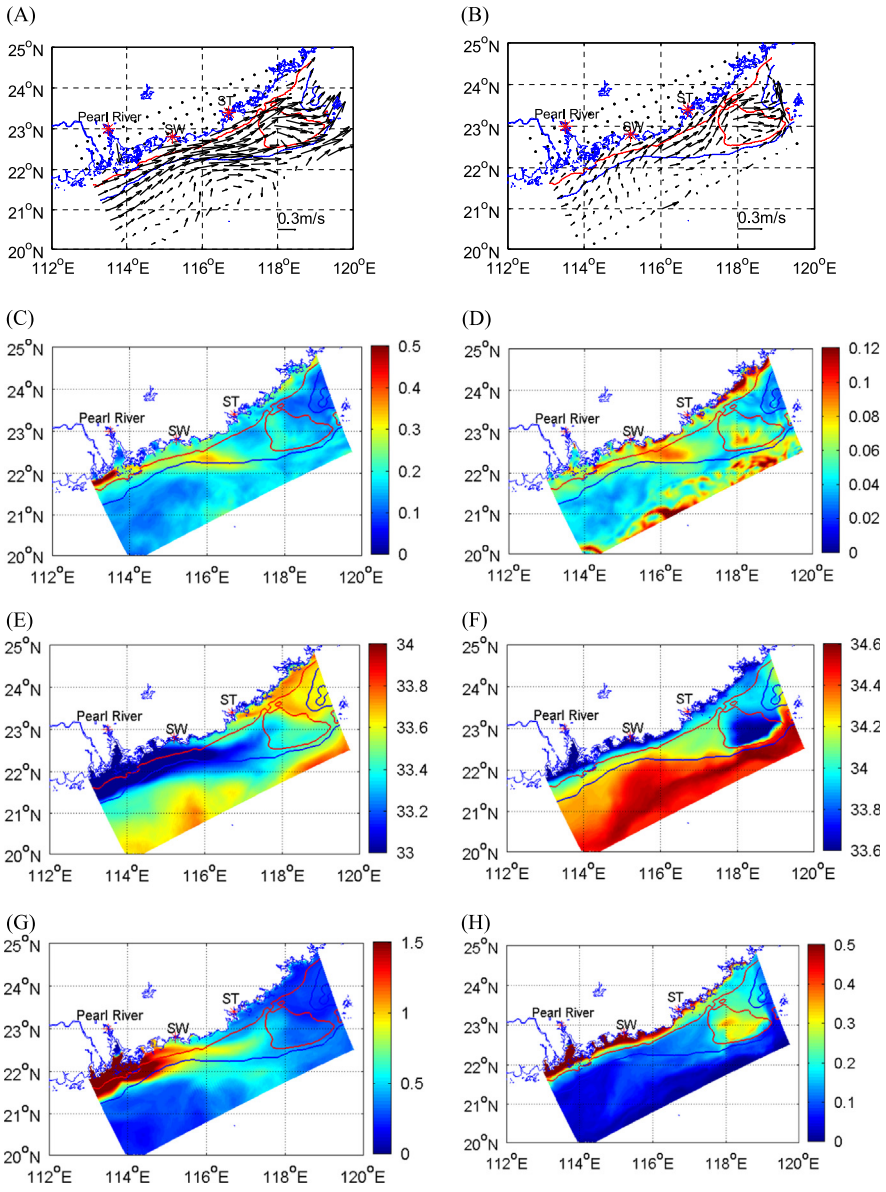

Fig. 8. Average surface and bottom velocity vectors (m s^{-1}) (a and b), velocity magnitude *std* (c and d), salinity (e and f); the salinity *std* (g and h) for days 20–100 (June 5–August 24). Strong shoreward advection is evident near the convex isobaths at the head of the widened shelf as is the subsequently eastward advection of dense bottom water between Shanwei and Shantou during upwelling. The 30 m and 50 m isobaths are shown as red and blue contour lines, respectively. (For interpretation of the references to color in this figure legend, the reader is referred to the web version of this article.)

and salinity (S) averaged over the period of June 4–August 23 (Fig. 8).

Fig. 8a shows considerable alongshore variation of the upwelling currents in the NSCS. The mainly eastward shelf currents intensified and bifurcated into northern and southern components towards the Taiwan Shoals after they encountered the head of the widened shelf near Shanwei. Meanwhile, the bottom currents tended to veer shoreward, and a relatively strong shoreward bottom transport occurred near the head of the widened shelf crossing the 50 m isobath. Stronger flow variability occurred near the head of the widened shelf in both upper and bottom layers where velocity magnitude was large (Fig. 8b).

The surface and bottom salinity were characterized by the offshore movement of the Pearl River plume at the surface and the shoreward advection of the saline water at the bottom (Fig. 8e and f). Saltier surface water surfaced at the inner shelf off Shantou as a result of upwelling that was forced by the local coastal promontory (Gan and Allen, 2002; Gan et al., 2009a). A relatively strong shoreward advance of the saline deep water occurred at the bottom over the converging isobaths at the head of the widened shelf and was subsequently transported downstream over the inner shelf and upwelled near Shantou. A strong variation in the salinity was found along the pathway of the Pearl River plume at the surface, while a relatively large standard deviation was mainly observed along the coast and in the Taiwan Shoals at the bottom (Fig. 8g and h).

3.3. Variation of flow

According to temporal variation of wind stress, we divided the period from June 5 to August 24 into four phases: upwelling growth (UG), upwelling relaxation (UR), downwelling growth (DG), and downwelling relaxation (DR). The example for each classification are shown in Fig. 9. Since the spatial variation of

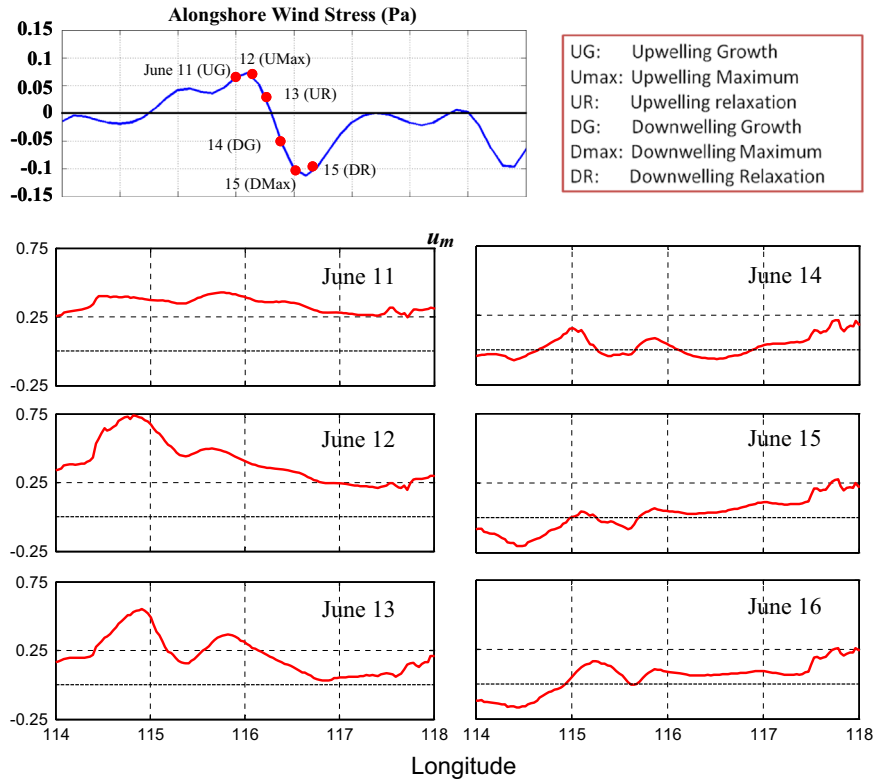

Fig. 9. Time series of alongshore wind stress (Pa, upper panel) and alongshore depth-integrated velocity (u_m, cm s^{-1}) averaged between the 30 m and 50 m isobaths (lower panel) from days 26–31 (June 11–16), including two days with maximum and minimum alongshore wind stress, respectively: that cover June 11 (UG), June 12 (Umax), June 13 (UR), June 14 (DG), June 15 (Dmax), and June 16 (DR). The dashed lines in the lower panel are the zero velocity lines.

wind stress over the shelf was relatively weak (Fig. 3), time series of wind stress at P1 was used as a reference. The variation of the upwelling circulation during these phases was examined in this subsection. In particular, we demonstrated the slowed retreat of upwelling during UR due to the widened shelf effect and the maintenance of the upwelling circulation during DG and DR due to downstream pumping.

3.3.1. *Upwelling relaxation*

The relaxation of upwelling circulation over the widened shelf in response to upwelling relaxation and downwelling winds is represented by alongshore depth-integrated velocity averaged between the 30 m and 50 m isobaths (u_m) as a function of alongshore distance from June 11 to 16 (Fig. 9). It covers the different stages of wind stress: June 11 (UG), 12 (Umax), 13 (UR), 14 (DG), 15 (Dmax), and 16 (DR). During the first two days, u_m was generally positive over the entire shelf and reached a maximum over the relatively narrow shelf around the head of the widened shelf (115.5°E) on June 12. Thus, $(\partial u_m/\partial x^*) < 0$ eastward of the head and the water mass converged over the widened shelf. x^* (> 0 northeastward) is the coordinate along the isobaths. As the wind relaxed after June 13, a stronger deceleration of the eastward current over the steeper and narrower shelf to the west of the head eventually led to $(\partial u_m/\partial x^*) > 0$, or divergence, over the widened shelf east of the head. Apparently, the different responses of alongshore current over the widened shelf tended to form a strong resistance to the reverse of the eastward velocity and sustained the pre-existing upwelling, as winds shifted to the downwelling favorable winds after June 14 (Fig. 9).

The processes in response to upwelling, upwelling relaxation, and downwelling winds over the shelf can also be identified by the evolution of velocity and tracers during different phases (Fig. 10). At Umax, the plume water (with salinity < 33.5) moved offshore and the saline water appeared along the coast to the east of the estuary. The bottom cold water (temperature < 23 °C) flowed upslope across the 50 m isobath and subsequently advected downstream over the shelf. One day later at UR, the plume became disconnected when the rate of discharge decreased to a minimum. The cold bottom water continued to advance shoreward, but both alongshore and onshore bottom currents weakened over the shelf. As the alongshore wind stress continued to drop at DG and Dmax, the bottom currents were weakened and turned seaward, but the basic structure of the bottom temperature remained largely unchanged. We noted that the currents flowed persistently eastward over the shelf during all phases, including DG and Dmax, and these eastward currents are the key to sustaining the basic upwelling structure (shown in Section 5).

3.3.2. *Upwelling during downwelling-favorable winds*

We further examined the variation of the upwelling circulation by showing the time-mean (June 5–August 24) wind stress, bottom salinity, and bottom current during the upwelling periods (UG and UR) and downwelling periods (DG and DR) for the entire season (Fig. 11), respectively. Surprisingly, we found little difference in the structures of the bottom currents and salinity between these two phases; they both exhibited distinct upwelling features except that the shoreward cross-isobath transport was weaker and the bottom salinity was smaller over the widened shelf during the downwelling. From a careful examination of the time series of velocity across the 50 m isobath for the entire period (Fig. 12), we found that, although the cross-shore currents generally flowed seaward in the upper layer and shoreward in the bottom layer

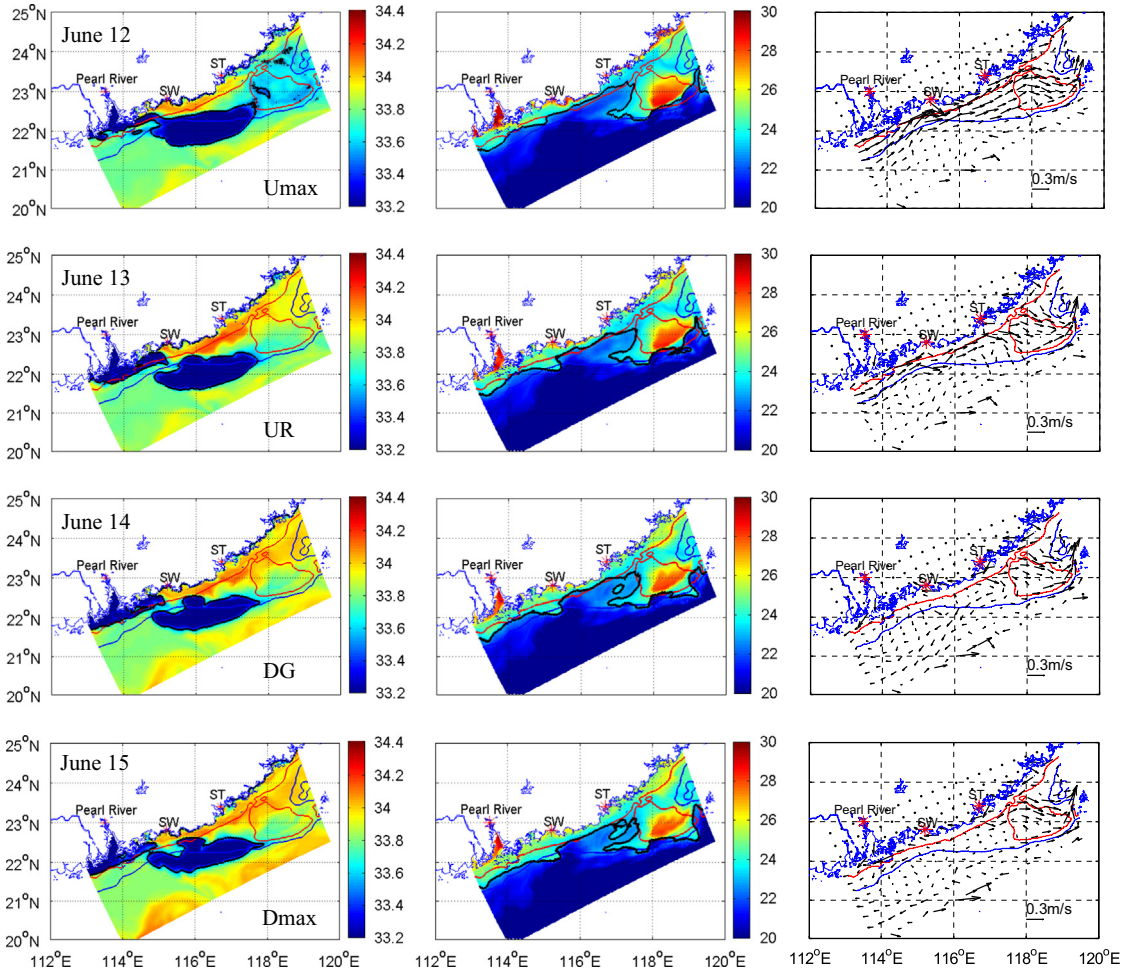

Fig. 10. Daily average surface salinity (left column), bottom temperature (°C, middle column), and bottom velocity vectors (m s^{-1}, right column) from days 27–30 (June 12–15): June 12 (Umax), June 13 (UR), June 14 (DG), and June 15 (Dmax). The black and bold contour lines represent the salinity and temperature of 33.5 and 23 °C, respectively. The 30 m and 50 m isobaths are shown as red and blue contour lines, respectively. (For interpretation of the references to color in this figure legend, the reader is referred to the web version of this article.)

during upwelling-favorable southwesterly (positive wind stress), strong shoreward currents occurred throughout the water column during the persistent downwelling-relaxation/downwelling winds between June 18 and 29 and between July 12 and 23 (marked by black horizontal boxes in Fig. 12). This led to upwelling during the downwelling favorable winds. The upwelling during these downwelling winds, in fact, was maintained by the presence of an eastward shelf current that interacted with the widened shelf to sustain the shoreward bottom frictional and geostrophic (i.e. along-isobath pressure gradient force) transports, or the essential upwelling dynamics over the shelf.

The origin of the eastward current over the shelf during the downwelling was induced by the increasing eastward volume flux downstream of the shelf near the Taiwan Strait. The eastward transport in the strait varied from 1.7 to 2.6 Sv during the entire period. Fig. 13 shows that the two positive peaks of the eastward transport anomaly (mean value ~2 Sv) were almost concurrent with the two upwelling events during the downwelling favorable winds. Our results indicate that the outflow anomaly in Taiwan Strait was partly induced by the relatively strong eastward winds in the strait; the outflow in the strait can also be caused by the northward component of Kuroshio intrusion through Luzon Strait (Gan et al., 2006). These findings suggest that the pumping by the outflow downstream of the widened shelf can maintain the alongshore eastward current and, thus, the upwelling dynamics over the widened shelf during downwelling relaxation/downwelling-favorable winds. The downstream flow influence on the shelf circulation has been observed by Gan et al. (2009a), in which a downwelling favorable wind induced by a tropical cyclone downstream of the shelf formed a westward current and suppressed wind-driven upwelling over the widened shelf.

4. Forcing mechanism

In order to show the forcing mechanism involved in the upwelling cross-isobath transport over the shelf, we present the time evolution of the momentum balances along the isobaths. We focus on the 30 days from June 11 to July 10, which cover the periods of upwelling and downwelling favorable winds. The momentum equation along the isobaths can be expressed as

$$u_t = -HADV - VADV + fv - \frac{1}{\rho}Py + HVIS + VVIS, \quad (1)$$

where (u,v) are along-isobath and cross-isobath depth-dependent velocities, and f is the Coriolis parameter. The terms in Eq. (1), from left to right, are acceleration, *ACCEL*; horizontal and vertical nonlinear advection, *HADV* and *VADV*, respectively; the Coriolis force, *COR*; the pressure gradient force, *PGF*; the horizontal viscous term, *HVIS* and the vertical viscous term, *VVIS*. It is also convenient to consider the sum of *COR* and *PGF*, which is referred to as the

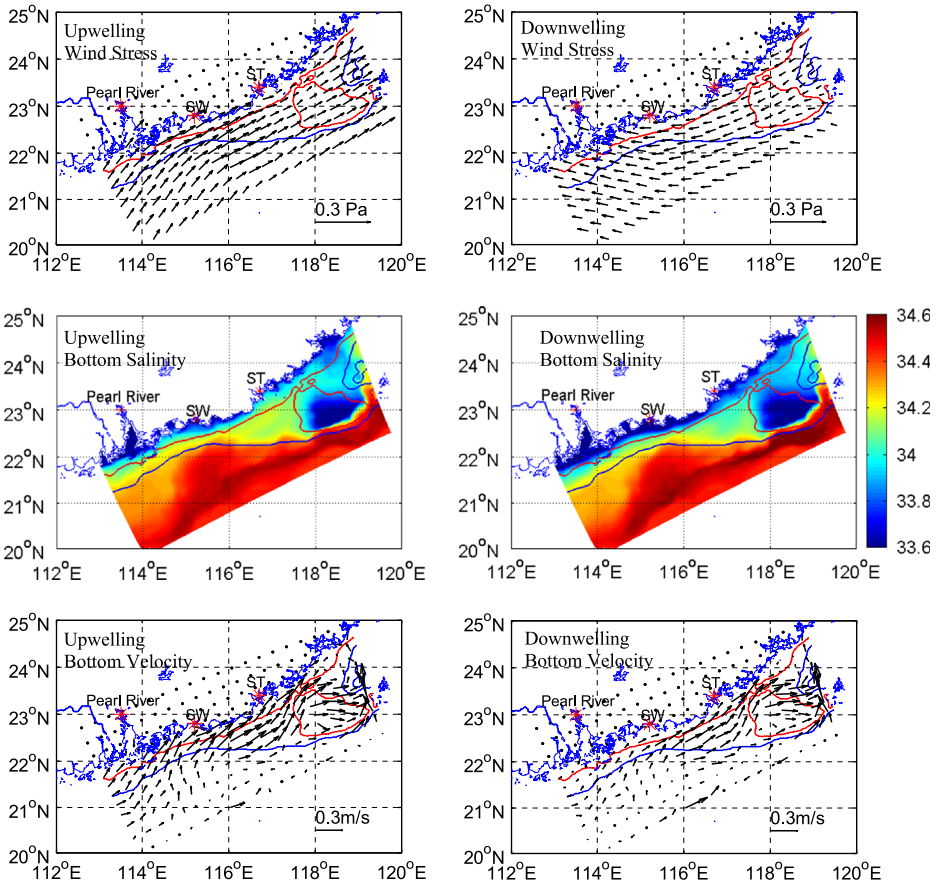

Fig. 11. Average of wind stress (Pa, 1st row), bottom salinity (2nd row), bottom current (m s^{-1}, 3rd row) for upwelling (UG and UR, left column) and downwelling (DG and DR, right column) from June 5 to August 24 (81 days). During this time, there are 25 days representing UG, 17 days representing UR, 20 days representing DG, and 19 days representing DR. The 30 m and 50 m isobaths are shown as red and blue contour lines, respectively. (For interpretation of the references to color in this figure legend, the reader is referred to the web version of this article.)

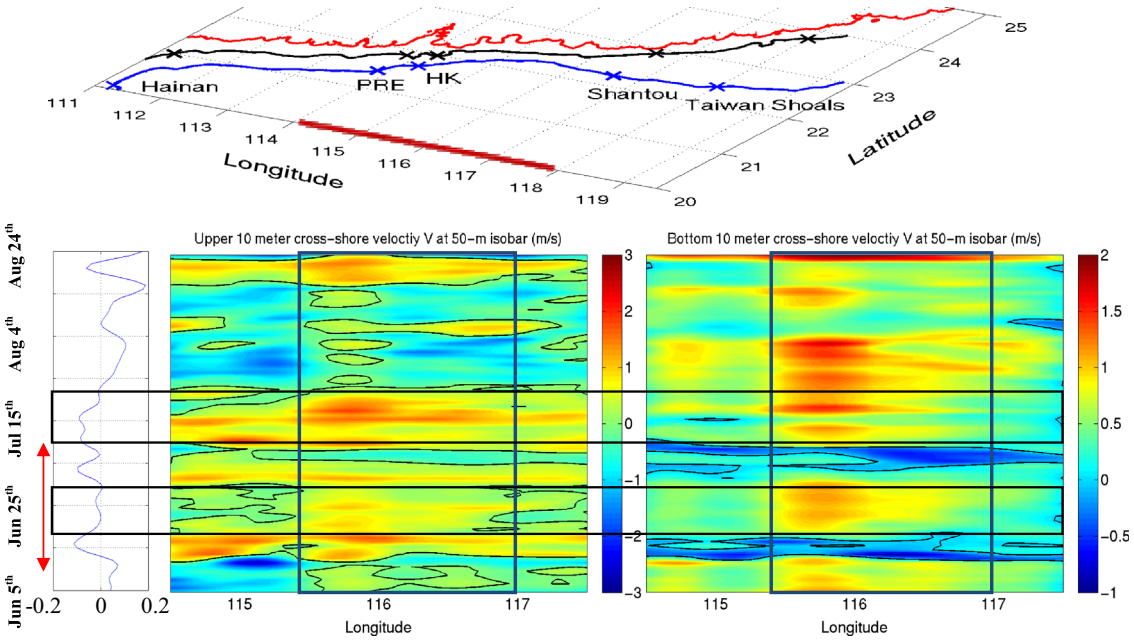

Fig. 12. Time and space dependent velocity across the 50 m isobath averaged in the upper 10 m layer (left) and bottom 10 m layer (right) over the widened shelf (114.5–117.5°E) from days 20 to 100 (June 5–August 24). The black contour lines represent zero cross-shore velocity. The time series of alongshore wind stress at location P1 (305,76) is shown next to the contour graphs. The locations of PRE, HK, Shantou, and the Taiwan Shoals are shown in the upper panel and the 30 m and 50 m isobaths are shown as black and blue contour lines, respectively. The region of the widened shelf is marked by the blue box and the periods of shoreward cross-isobath bottom currents during the downwelling winds are marked by the black boxes. The time period (June 10–July 10), marked by the red arrow on the left, is the period selected for the analysis of the momentum balance presented in Fig. 14. (For interpretation of the references to color in this figure legend, the reader is referred to the web version of this article.)

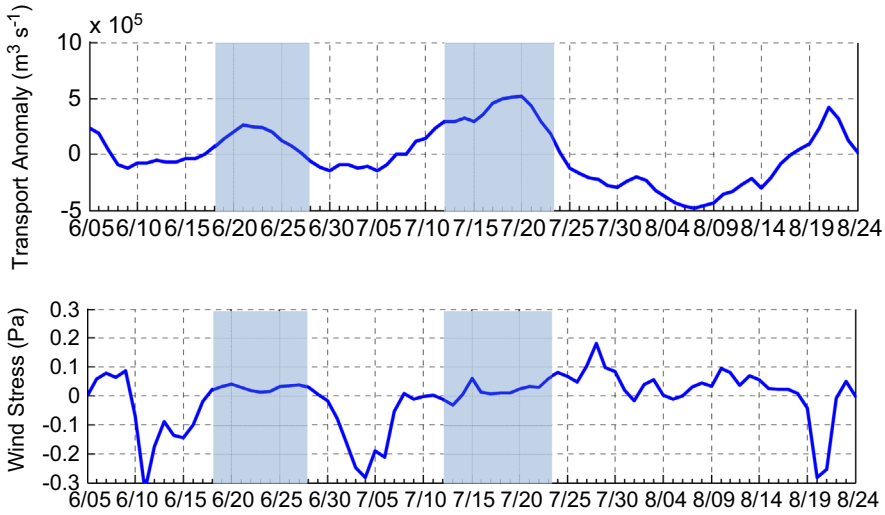

Fig. 13. Time series of (upper panel) eastward transport anomaly ($m^3\ s^{-1}$) and (lower panel) average alongshore wind stress (Pa) across Taiwan Strait. Two shaded boxes mark the periods of the positive transport anomaly that correspond to the two periods with downwelling/downwelling relaxation winds on June 18–30 and July 12–25, respectively. The mean value of the eastward transport is ~2 Sv.

ageostrophic pressure gradient, *AGE*:

$$AGE = fv - \frac{1}{\rho}Py, \tag{2}$$

because *AGE* is the net difference between the pressure gradient (*PGF*) and the Coriolis force (*COR*), the sign of *AGE* reflects the residual of geostrophy, either from the Coriolis force (*COR*) or from the pressure gradient (*PGF*).

The terms in Eq. (1) along the 50 m isobath were averaged over the bottom 10 m layer (Fig. 14) to effectively show the forcing of the geostrophic flow and bottom Ekman flow. These two flows were the key indicators of the intrinsic upwelling dynamics over the widened shelf in the NSCS as shown in Gan et al. (2009a). The Coriolis force from the shoreward/seaward cross-isobath velocity (*COR*) was balanced by negative/positive *PGF* and was positively correlated with the current deceleration/acceleration (*ACCEL*). *AGE* was primarily balanced by the vertical viscous term (*VVIS*) to form Ekman velocity. In general, *HADV* was larger than *VADV* although they appeared to balance each other when the mass fluxes were contained in these two terms. The nonlinear effect contributed little to the cross-shelf transport. It is clear that the shoreward cross-isobath transport ($COR > 0$) over the widened shelf was caused by the negative along-isobath *PGF* and *VVIS* during upwelling winds from June 11 to 13 as well as during the prolonged downwelling relaxation/downwelling winds from June 18 to 30. Only when the downwelling-favorable wind was strong enough, for example, around June 16 and July 4, the positive *COR* and shoreward Ekman transport were absent. While the intensified Ekman velocity was induced by the strengthened currents near the head of the widened shelf, the mechanism for the geostrophic cross-isobath transport contributed by *PGF* was not as obvious. Recently, Gan et al. (2013), based on the linear depth-integrated vorticity equation, found that the depth-averaged *PGF* or PGF_m was, in fact, formed by the net stress curl in the water column when stratification was weak:

$$PGF_m = \frac{\nabla \times \tau_b - \nabla \times \tau_s}{\rho_o H_{x^*}}. \tag{3}$$

Here, H is the water depth over the shelf and H_{x^*} is the seaward differentiation of H in cross-isobath coordinates x^*; τ_s and τ_b are wind stress and bottom stress, respectively. The time series of PGF_m (Fig. 15) was well-correlated with the *PGF* integrated in the bottom 10 m layer (Fig. 14), and the overall greater contribution of bottom stress curl to PGF_m was reflected by $\left|\frac{\nabla \times \tau_b}{\nabla \times \tau_s}\right| > 1$. When wind stress curl is weak and bottom stress is linearly linked with bottom velocity, it becomes

$$PGF_m = \frac{c_d |v_b| \nabla \times v_b}{H_{x^*}}, \tag{4}$$

where c_d is the frictional drag coefficient and v_b is the bottom velocity. Eq. (4) stated that the PGF_m can be formed as a result of bottom vorticity. Thus, a strong negative shear vorticity on the seaside of the upwelling jet core (Fig. 8) provided the vorticity source for the formation of the intensified negative PGF_m over the widened shelf. It is clear that as long as there existed an alongshore eastward current, as in the cases of upwelling/upwelling relaxation (June 11–13) and downwelling relaxation/downwelling (June 18–30), the alongshore current formed the cross-isobath shoreward upslope motion from bottom Ekman transport and from geostrophic transport induced by the negative shear vorticity offshore of the eastward current. The amplified currents near the head of the widened shelf with converging isobaths enhanced these effects (Fig. 14). Unlike the pre-existing upwelling circulation during upwelling relaxation winds, the upwelling during the downwelling relaxation/downwelling-favorable winds was rebuilt by the eastward current due to the positive anomaly of eastward flux downstream of the shelf.

5. Dynamics sensitivity

We conducted four sensitivity experiments in order to further explore the features of the spin-up and spin-down processes of the upwelling circulation in relation to winds and lateral flux forcing from remote boundaries. We provide a brief description and abbreviations for the four experiments in Table 1.

We chose a typical upwelling circulation for the 30-day period from July 16 to August 14, from the original model results, to be the standard case or Experiment 1 (CU, Fig. 16a). The time-averaged transports from June 6 to August 24 (Fig. 3) in the southern and eastern boundaries were utilized as steady lateral flux in the sensitivity experiments in order to better isolate the concerned responses. We compared the time series of transport across the 50 m isobath in the upper and bottom frictional layers

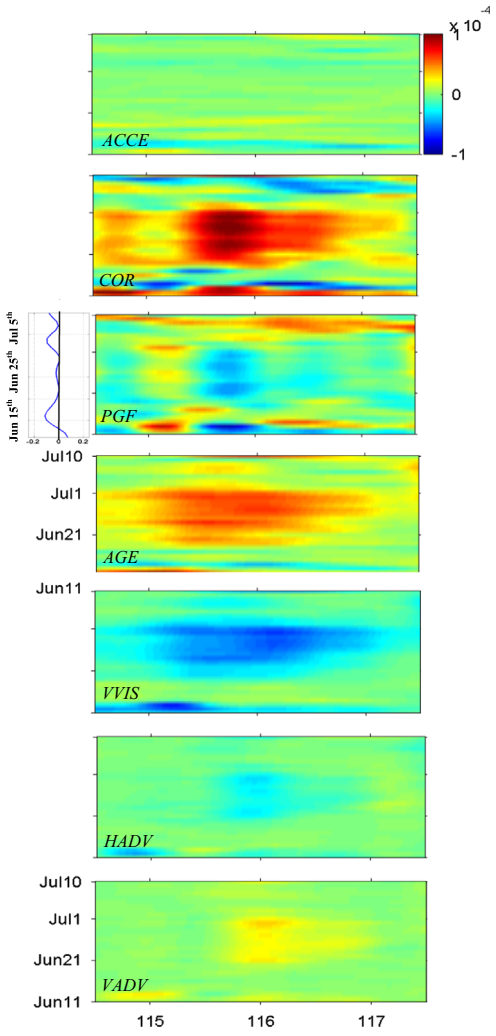

Fig. 14. Time series of momentum term balance (m s^{-2}) integrated in the bottom 10 m layer along the 50 m isobaths between 114.5°E and 117.5°E from days 26 to 55 (June 11–July 10): June 11 (UG), June 12 (Umax), June 13 (UR), June 14 (DG), June 15 (Dmax) and June 16 (DR). From top to bottom, they represent acceleration (ACCEL), Coriolis force (*COR*), pressure gradient force (*PGF*), ageostrophic pressure gradient (*AGE*), vertical viscous force (*VVIS*), horizontal nonlinear advection (*HADV*), and vertical nonlinear advection (*VADV*). The magnitude of the horizontal viscosity is so small that its effect can be neglected (not shown). The time series of alongshore wind stress (Pa) at location P1 (305,76) is shown next to the *PGF*. The dominant balance during the whole period is the geostrophic balance between *COR* and *PGF*, whereas *AGE* is mainly balanced by the *VVIS* because of the bottom Ekman balance.

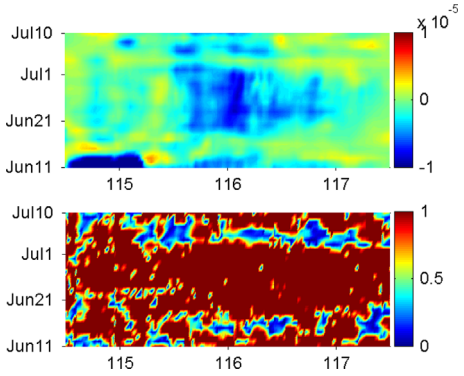

Fig. 15. Time series of (top panel) depth-averaged pressure gradient force (m s^{-2}) obtained from bottom and surface stress curls as in Eq. (3), and of (bottom panel) absolute value of ratio between bottom stress curl and wind stress curl, along the 50 m isobath between 114.5°E and 117.5°E from days 26 to 55 (June 11–July 10).

and in the interior layers among these sensitivity cases to identify forcing processes in the upwelling circulation.

Experiment 2 (WE, Fig. 16b) examined the wind forcing effect. The wind stress was set to zero over the whole domain for the 30-day period and the other parameters remained unchanged. The results show that the upslope transports remained but weakened in the middle and bottom layers during the entire 30 days, although the offshore transport in the upper layer was very small. The transports in WE and CU varied differently in time. In CU, the transport in the upper/bottom layers correlated negatively/positively with the wind stress (Fig. 3) and the transport in the middle layer had stronger variability. In WE, the variability in these three layers was weakened. The persistent but weakened shoreward transport, when upwelling wind forcing was absent over the entire shelf, was sustained by the eastward flux in the eastern boundary. The comparison of WE and CU clearly showed that the variance of the upwelling was mainly determined by the local wind forcing.

As part of the SCS basin circulation along the continental margin during the southwesterly monsoon (Gan et al., 2006), the current from the basin circulation may intrude into the NSCS from the southern boundary and enhance the intensity of the along-shelf flow. Experiment 3 (SBE, Fig. 16c) examined the control of this southern influx by increasing the intrusive velocities along the southern boundary to 1.5 times their original values. With the increase of the northeastward currents into the domain from the south, the upwelling effect would become stronger due to an increase of eastward transport over the widened shelf. Surprisingly, there was little change in the cross-isobath transport in the bottom layer after the enhancement of flux at the southern boundary. It slightly increased the shoreward cross-isobath transport in the middle layer and the transport was moved seaward in the upper layer. Our results show that the intrusive currents from the southern boundary were mainly re-circulated back towards the basin along the southern boundary, and only a very small portion of the intrusive currents eventually reached the shelf and exited the eastern boundary.

Experiment 4 (EBE, Fig. 16d) examined the control of the upwelling by pumping at the eastern boundary. Similar to SBE, the velocities along the eastern boundary of the Taiwan Strait (Fig. 1), which were mainly eastward, were increased to 1.5 times their original values in EBE. With more water being pumped out of the domain, the transport across the 50 m isobath in EBE was substantially increased in the middle and bottom layers. This effectively increased the intensity of the upslope transport of the deep water during the upwelling.

6. Summary and conclusion

Coastal circulation is highly space and time dependent and is subject to the joint controls of spatiotemporal variations of wind, remote forcing, and the intrinsic dynamics arising from the interaction between the forced current and shelf topography. In this study, we investigated the variability of distinct upwelling circulation, with particular regard to the formation, maintenance, and relaxation of upwelling circulation in response to upwelling favorable wind, downwelling favorable wind, and remote forcing over the unique widened shelf in the NSCS. We utilized field measurements and a three-dimensional, downscaling model to identify the processes and dynamics that govern the upwelling circulation.

With the presence of a strong westward pressure gradient force and an enhanced shoreward bottom Ekman transport over the widened shelf, the pre-existing upwelling circulation cannot be easily impeded by the generally weak and short duration

Table 1
Summary of experiments that tested the effects of wind forcing and volume fluxes at the southern boundary and eastern boundary on the upwelling cross-shore transport, respectively.

Experiment	1	2	3	4
Description	Characterized upwelling from model result (standard case)	Wind effect (no wind)	Southern boundary effect (1.5 times of the original SBT transport)	Eastern boundary effect (1.5 times of the original EBT pumping)
Abbreviation	CU	WE	SBE	EBE

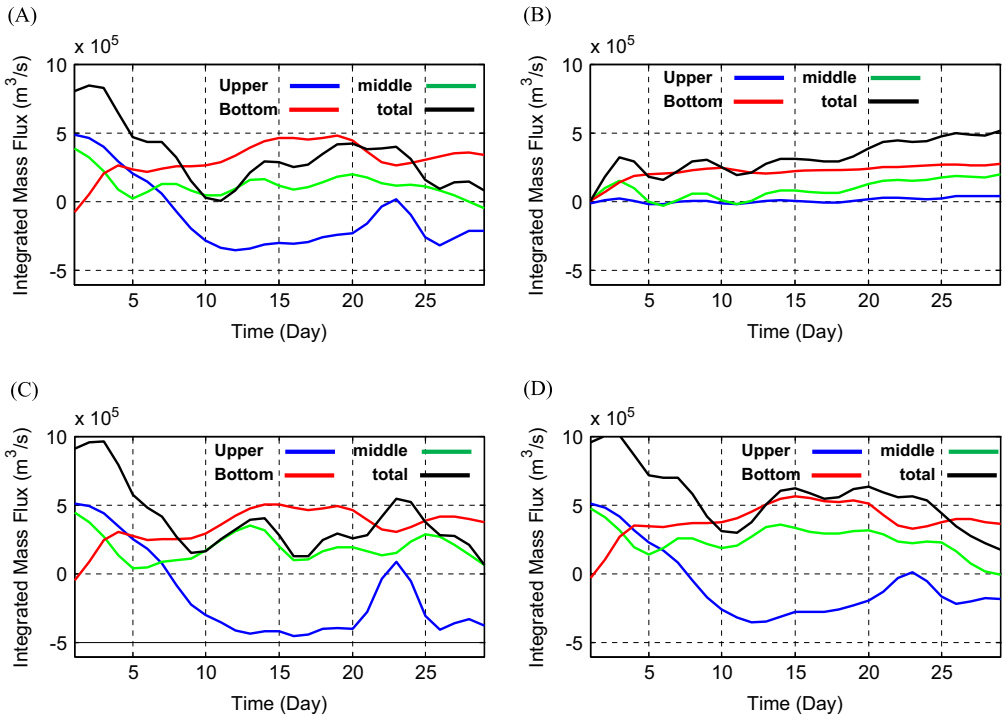

Fig. 16. Comparisons among experiments 1–4 using the time series of transport across the 50 m isobath in the upper (upper 10 m), middle (10 m < depth < 40 m) and bottom (bottom 10 m) layers over the widened shelf during July 16–August 14. CU (a), WE (b), SBE (c) and EBE (d) are the cases of standard, no wind, increased fluxes in the southern and eastern boundaries, respectively.

downwelling winds during summer because of the slow retreat of the pre-existing upwelling dynamic layout over the broad widened shelf topography.

Upwelling can be formed over the NSCS shelf by the existence of an eastward flow that activates the interaction of the flow with the widened shelf topography to form the shoreward geostrophic and bottom Ekman transports. Thus, the upwelling over the widened shelf may be generated during the downwelling-favorable or downwelling-relaxation winds as long as the eastward flow remains over the widened shelf. This was the case in the NSCS during the summer of 2000 and is expected to constantly occur due to the eastward pumping by the prevailing eastward transport in the southwest opening of Taiwan Strait during summer.

The momentum flux downstream of the shelf can change the intensity of the alongshore current over the shelf, and, thus, the dynamics arising from the interaction of the flow with the shelf topography. The spatial heterogeneity of wind forcing and the intrusion of the Kuroshio from Luzon Strait can form an eastward flux downstream of the shelf. The flux can be strong enough to maintain the eastward flow over the shelf for the upwelling to occur, even when the local wind forcing is downwelling-favorable over the shelf. On the other hand, the momentum flux from the interior of the SCS basin had a relatively small effect on the shelf circulation because most of the intrusive transports recirculated seaward. It appears to be difficult for the influx from the southern boundary to reach the nearshore shelf by crossing the isobaths over the broad NSCS shelf. The formation, maintenance, and relaxation of upwelling over the widened shelf in the NSCS are controlled by the integrated forcing processes that support the intrinsic upwelling dynamics over the shelf. This is expected to occur in other coastal oceans around the world.

Acknowledgments

This research was supported by Hong Kong's Research Grant Council under Projects N_HKUST627/13 and GRF612412.

References

Barth, J.A., Pierce, S.D., Castelao, R.M., 2005. Time-dependent, wind-driven flow over a shallow mid-shelf submarine bank. J. Geophys. Res. 110, C10S05, http://dx.doi.org/10.1029/2004JC002761.

Castelao, R.M., Barth, J.A., 2007. The role of wind-stress curl in jet separation at a cape. J. Phys. Oceanogr. 37, 2652–2671.

Chapman, David C., 1987. Application of wind-forced, long, coastal-trapped wave theory along the California coast. J. Geophys. Res. 92 (C2), 1798–1816.

Denbo, D.W., Allen, J.S., 1987. Large-scale response to atmospheric forcing of shelf currents and coastal sea level off the west coast of North America: May–July 1981 and 1982. J. Geophys. Res. 92 (C2), 1757–1782, http://dx.doi.org/10.1029/JC092iC02p01757.

Gan, J.H.S., Ho, Liang, L., 2013. Dynamics of intensified downwelling circulation over a widened shelf. J. Phys. Oceanogr. 43 (1), 80–94, http://dx.doi.org/10.1175/JPO-D-12-02.1.

Gan, J., Allen, J.S., 2002. A modeling study of shelf circulation off northern California in the region of the Coastal Ocean dynamics experiment: response to relaxation of upwelling winds. J. Geophys. Res. 107 (C9), 3123, http://dx.doi.org/10.1029/2000JC000768.

Gan, J., Allen, J.S., 2005a. Modeling upwelling circulation off the Oregon coast. J. Geophys. Res. 110, C10S07, http://dx.doi.org/10.1029/2004JC002692.

Gan, J., Allen, J.S., 2005b. On open boundary conditions for a limited area coastal model off Oregon. Part 1: response to idealized wind forcing. Ocean Modell. 8, 115–133, http://dx.doi.org/10.1016/j.ocemod.2003.12.006.

Gan, J., Allen, J.S., Samelson, R.M., 2005. On open boundary conditions for a limited-area coastal model off Oregon. Part 2: response to wind forcing from a regional mesoscale atmospheric model. Ocean Modell. 8, 155–173, http://dx.doi.org/10.1016/j.ocemod.2003.12.007.

Gan, Cheung, Guo, Li, 2009a. Intensified upwelling over a widened shelf in the northeastern South China Sea. J. Geophys. Res. 114, C09019.

Gan, J., Li, L., Wang, D., Guo, X., 2009b. Interaction of a river plume with coastal upwelling in the northeastern South China Sea. Cont. Shelf Res. 29, 728–740, http://dx.doi.org/10.1016/j.csr.2008.12.002.

Gan, Lu, Dai, Cheung, Liu, Harrison, 2010. Biological response to intensified upwelling and to a river plume in the northeastern South China Sea: a modeling study. J. Geophys. Res. 115, C09001, http://dx.doi.org/10.1029/2007JC004660.

Gan, J., Li, H., Curchitser, E.N., Haidvogel, D.B., 2006. Modeling South China Sea circulation. Response to seasonal forcing regimes. J. Geophys. Res. 111, C06034, http://dx.doi.org/10.1029/2005JC003298.

Janowitz, G.S., Pietrafesa, L.J., 1982. The effects of alongshore variation in bottom topography on a boundary current, or, topographically induced upwelling. Cont. Shelf Res. 1 (2), 123–141.

Lentz, S.J., Guza, R.T., Elgar, S., Feddersen, F., Herbes, T.H.C., 1999. Momentum balances in the North Carolina inner shelf. J. Geophys. Res. 104 (18), 205–226.

Li, L., 1993. Summer upwelling system over the northern continental shelf of the South China Sea: a physical description. In: Jilan, S., Chuang, W.-S., Hsueh, R. (Eds.), Proceedings of the Symposium on the Physical and Chemical Oceanography of the China Seas. China Ocean, Beijing, pp. 58–68.

Mellor, G.L., Yamada, T., 1982. Development of a turbulence closure model for geophysical fluid problems. Rev. Geophys. 20, 851–875.

Oke, P.R., Middleton, J.H., 2000. Topographically induced upwelling off Eastern Australia. J. Phys. Oceanogr. 30, 512–531.

Pringle, J., 2002. Enhancement of wind-driven upwelling and downwelling by alongshore bathymetric variability. J. Phys. Oceanogr. 32, 3101–3112.

Pringle, J.M., Dever, E.P., 2009. Dynamics of wind-driven upwelling and relaxation between Monterey Bay and Point Arena: local-, regional-, and gyre-scale controls. J. Geophys. Res. 114, C07003, http://dx.doi.org/10.1029/2008JC005016.

Send, U., Beardsley, R.C., Winant, C.D., 1987. Relaxation from upwelling in the Coastal Ocean dynamics experiment. J. Geophys. Res. 92, 1683–1698.

Shchepetkin, A.F., McWilliams, J.C., 2005. The regional oceanic modeling system (ROMS): a split-explicit, free-surface, topography following coordinate oceanic model. Ocean Modell. 9, 347–404.

Weisberg, R.H., Black, B.D., Li, Z., 2000. An upwelling case study on Florida′s west coast. J. Geophys. Res. 105 (11), 459–469.

Weisberg, R.H., He, R., Liu, Y., Virmani, J.I., 2005. West Florida shelf circulation on synoptic, seasonal, and inter-annual time scales. In: Sturges, W., Lugo-Fernandez, A. (Eds.), Circulation in the Gulf of Mexico: Observations and Models, AGU Monograph Series, Geophysical Monograph, vol. 161, pp. 325–347.